This paper must be cited as:
Cardoso, M.A., Correia, S.F.H., Gonçalves, H.M.R. *et al.* Solar spectral management with electrochromic devices including PMMA films doped with biluminescent ionosilicas. *J Sol-Gel Sci Technol* **101**, 58–70 (2022). https://doi.org/10.1007/s10971-021-05612-z

Solar spectral management with electrochromic devices including PMMA films doped with biluminescent ionosilicas

Marita A. Cardoso[1,2], **Sandra F. H. Corrreia**[1], **Helena M. R. Gonçalves**[2,3], **Rui F. P. Pereira**[4], **Sónia Pereira**[5], **Teresa M.R. Maria**[6], **Maria M. Silva**[4], **Artur J. M. Valente**[6], **Elvira Fortunato**[5], **Rute A. S. Ferreira**[1*] (ORCID: 0000-0003-1085-7836), **Verónica de Zea Bermudez**[2*](ORCID: 0000-0002-7577-4938)

[1] Department of Physics and CICECO-Aveiro Institute of Materials, University of Aveiro, 3810-193 Aveiro, Portugal

[2] Chemistry Department and CQ-VR, University of Trás-os-Montes e Alto Douro, 5000-801 Vila Real, Portugal

[3] REQUIMTE, Instituto Superior de Engenharia do Porto, 4200-072 Porto, Portugal

[4] Chemistry Center, University of Minho, 4710-057 Braga, Portugal

[5] i3N/CENIMAT, Department of Materials Science, Faculty of Sciences and Technology, New University of Lisbon, Campus de Caparica, 2829-516 Caparica, Portugal

[6] University of Coimbra, CQC, Chemistry Department, 3004-535 Coimbra, Portugal

Abstract 150-250

The technological potential of poly(methyl methacrylate) (PMMA)-based composite films doped with lanthanide-doped sol-gel derived ionosilicas (IS-Ln) previously proposed for luminescent down-shifting (LDS) and luminescent solar concentrators (LSC) layers connected to photovoltaic (PV) cells is extended here to electrochromic devices (ECDs), targeting the fabrication of single energy harvesting/conversion/management LSC-LDS/PV/ECD systems. These integrated devices have foreseen application in the windows of future zero-energy buildings of smart cities. The proof-of-concept is given with the report of the electro-optical performance of an ECD comprising an optimized electrolyte film composed of PMMA, IS-Nd and IS-Eu, and the 1-butyl-3-methylimidazolium hexafluorophosphate ionic liquid. This amorphous electrolyte is stable below 160 ºC, exhibits high ionic conductivity (2.13×10^{-4} and 8.76×10^{-4} S cm^{-1} at room temperature and 44 ºC, respectively), and emits in the visible (red color) and near-infrared (NIR) spectral regions. The device demonstrated fast switching speed (50 s) and high transparency in the visible-to-NIR spectral regions (transmittance (T) = 79/96/89/77% at 555/1000/1500/1650 nm in the as-prepared state, respectively). Upon application of ± 2.5 V for 200 cycles, at the same wavelengths the $T_{bleached}/T_{colored}$ values were 44/28, 46/26, 39/20 and 27/9 %, respectively, and the coloration efficiency (CE) values CE_{in}/CE_{out} values were −302/+181, −381/+228, −446/+267 and −734/+440 cm^2 C^{-1}, respectively.

Graphical Abstract

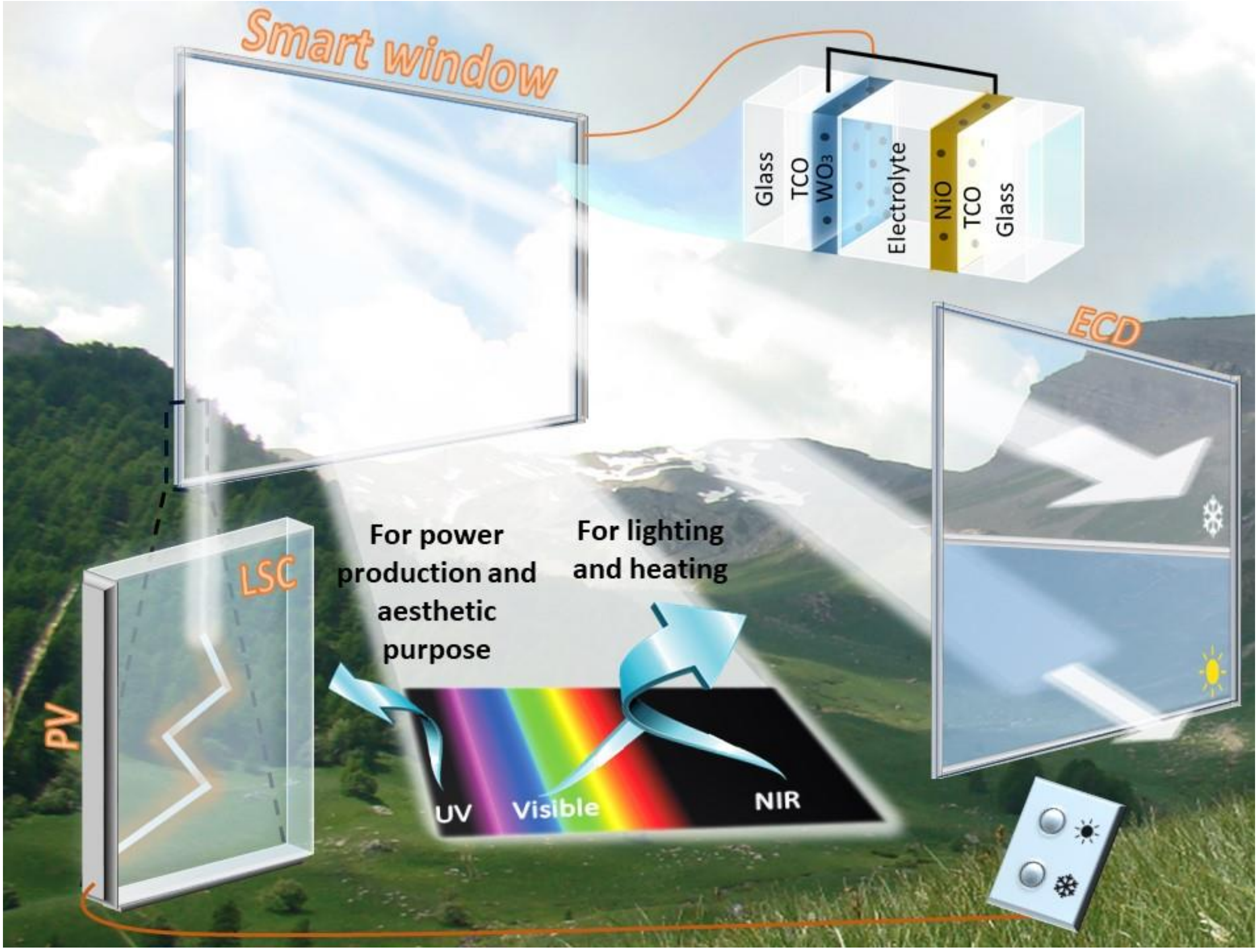

Keywords • sol-gel • imidazolium-based ionosilicas • Eu^{3+} and Nd^{3+} complex anions • poly(methyl methacrylate) • 1-butyl-3-methylimidazolium hexafluorophosphate • electrochromic smart windows • zero energy buildings

Highlights

- Red-emitting ECDs enabling dynamic control of sunlight and offering uninterrupted heat emission were fabricated.
- The ECD electrolyte composition was based on the formulation used previously for films acting both as LDS and LSC layers.
- The electrolyte included PMMA, $Nd^{3+/}Eu^{3+}$-doped ionosilicas, and 1-butyl-3-methylimidazolium hexafluorophosphate.
- The electrolyte is amorphous, exhibits good ionic conductivity, and emits in the visible (red color) and NIR regions.
- The ECD performance proves its applicability in an integrated LSC-LDS/PV/ECD system.

1 Introduction

The increasing energy needs of modern societies and fossil fuels growing consumption, which are directly responsible for greenhouse gas (GHG) emissions and its deleterious consequences (global warming and climate changes), are critical issues that must be tackled urgently. If not, the situation will worsen, as it is estimated that by 2050 more than 6 billion people will live in urban areas. In Europe, a highly urbanized continent, the densification of population in cities will seriously threaten livability. The smart city concept emerged as a response to the challenges for urban development, promising to offer citizens better lives, while meeting climate and energy goals, reducing environmental impact, and acting as an economic growth key driver.

Smart cities require smart, sustainable and energy-efficient buildings. In the European Union (EU) buildings (residential or not) are the largest energy consumer and one of the largest CO_2 emitters, being responsible for 40% of energy consumption and 36% of GHG emissions [1]. Half of the energy consumption in a building corresponds to the power spent on heating, ventilation, air-conditioning, and artificial lighting. The recognition that the building sector is a key pillar of the energy solution [2] led to the so-called Nearly Zero Energy Building (NZEB) concept, which envisages converting buildings into renewable energy sources where all the energy used throughout the year must equal the renewable energy created on-site or by renewable energy sources. The large-scale deployment of NZEBs is fostered to ensure the sustainability of the European society and economy for the building sector [3].

Buildings energy performance is a top priority issue for energy policies in the EU. Three European directives stimulate the transition to decarbonized buildings: (1) The 2020 Climate and Energy Package [1] (associated with the Renewable Energy Directive [4]), the Energy Efficiency Plan [5], and the Energy Efficiency Directive [6]), which targets a 20% cut in GHG emissions (from 1990 levels), 20% of energy from renewables, and 20% improvement in energy efficiency; (2) The 2030 Climate and Energy Framework [7], which targets 40% cuts in GHG emissions (from 1990 levels), 32% share for renewable energy, and 32.5% improvement in energy efficiency; (3) The 2050 Long-Term Strategy [8], which targets climate-neutrality by 2050 and net-zero GHG emissions. These objectives are in line with the European Green Deal [9] and the Paris Agreement on climate change.

At a worldwide scale, the United Nations (UN) Sustainable Development Goals 7 – Affordable and Clean Energy, 11 – Sustainable Cities and Communities, and 13 – Climate Action [10] aim to make cities inclusive, safe, resilient and sustainable, to ensure universal access to affordable, adequate, safe and sustainable housing and modern energy for all, and thus provide better well-being, safety, less climate changes and its impacts, and more economic progress. In July 2020 the UN Secretary-General asked world leaders to choose the "clean energy path" and boost the use of renewables in the post-pandemic economic recovery plans [11]. To achieve these goals new energy materials and new energy-efficient technologies are mandatory.

In buildings, the envelope (external walls, floors, roofs, ceilings, windows, and doors) is responsible for more than 30% of the consumed energy. Windows are of particular interest since they impact dramatically on the mitigation of the building energy consumption. Transitioning from static to dynamic (smart) windows is extremely beneficial [12], reducing the building's energy needs by about 40 % [13]. Dynamic windows allow adjusting the sunlight (visible radiation) and solar heat (near-infrared (NIR) radiation) inflow in real time, at the occupant's choice, independently of the geographical location, climate region, season of the year, or room's orientation, increasing the building energy performance by minimizing heating and cooling needs indoors, providing more visual and thermal comfort, and improving outdoors view. Since ca. 44 and 49% of the solar energy lies in the visible and NIR regions, respectively, (**Fig. 1**) the incorporation of visible and NIR blocking/admission functions in smart windows has become mandatory to ensure high energy efficiency [14-22].

Among the available smart window technologies, electrochromic windows (ECWs) offer huge potential for the solar spectrum management and therefore for the fabrication of architectural large-area glazing of NZEBs [2, 23-25]. ECWs are multilayer sandwich-type battery-like devices in which the application of a small voltage (< 3 V) triggers a reversible change in the color of one (or two) EC layer(s). Sunlight modulation over a broad spectral range, controllable transmission, absorption, and/or reflectance, open circuit memory, and non-obstruction of outside view during operation, are some of the major benefits of ECWs [26, 27].

Recently some of us introduced EC devices (ECDs) enabling control of the visible and NIR spectral regions of the solar spectrum [19, 21, 28]. The rational of the new ECD design was to combine visible-to-NIR transparent conducting oxide (TCO) external layers with a suitable electrolyte. A sustainable three-mode modulation ECD with unprecedented figures of merit was produced using amorphous zinc-doped indium oxide (a-IZO) [29]) TCO layers and a sol-gel derived electrolyte (DUPIL$_{60}$) based on a di-ureasil host hybrid matrix doped with the *N*-butylimidazolium trifluoromethanesulfonate ([BIm][TfO]) proton ionic liquid (PIL) [28]. The device, comprising cathodically coloring amorphous tungsten oxide (a-WO_3) and anodically coloring crystalline nickel oxide (c-NiO), featured colossal coloration efficiency (CE), excellent cycling stability, and remarkable memory effect [28].

In the present work the above ECD concept has been taken to the next level. ECDs enabling dynamic control of light, offering uninterrupted red color and heat emission, have been developed. Motivated by the fact that ECWs can operate alone or paired with other technological solutions, such as solar cells [30] and building integrated photovoltaics (BIPVs) [31], the composition of the present ECD electrolytes relied on the formulation we recently proposed for luminescent solar concentrator (LSC) [32-34] and luminescent down-shifting (LDS) [32] layers. We recall that LSC and LDS layers increase PV cell's UV response by down-shifting short wavelength solar radiation to longer wavelengths where the absorption of the solar cell is higher [34-40]. The energy of the converted photons is resonant with the absorption curves of PV devices (**Fig. 1**).

The developed LSC and LDS layers [32, 33] included a poly(methyl methacrylate) (PMMA)-based system doped with lanthanide (Ln)-doped ionosilicas (ISs) (noted as IS-Ln-X, where X = IS-Ln/PMMA w/w) prepared by the sol-gel method. In these luminescent materials the IS compound comprised a silica matrix covalently bonded to 1-butyl-3-propyl-imidazolium cations via the propyl chain. The positive charge of this pendant organic group was counterbalanced by the complex ion $[Ln(tta)_4]^-$, where tta^- is 2-thenoyltrifluoroacetonate and Ln = Nd^{3+}, Eu^{3+}, Tb^{3+}, and Yb^{3+}. With respect to the neutral complex, the presence of an additional tta^- ligand adds two extra carbonyl oxygen atoms to the first coordination sphere of the Ln^{3+} ion, reducing quenching effects, enhancing the quantum efficiency values, and increasing the photo-, mechanical, and thermal stability. PMMA, a material typically employed in LSC and LDS layers, was chosen as host polymer matrix on account of its attractive properties: high optical transparency under solar irradiation, high thermal stability (−70-100 °C), low cost, non-toxicity, high scratch resistance, superb high resistance to UV radiation exposure and several chemical treatments, exceptional performance in all-weather conditions, higher impact resistance than glass, easy handling and processing, and great compatibility with liquid electrolytes, such as ILs [41].

Despite the well-known photobleaching typical of some organic ligands, the incorporation of beta-diketonate complexes into PMMA or di-ureasils hosts is known to increase their photostability [42-45]. Furthermore, studies on their stability at strict accelerated aging tests were done under controlled temperature and relative humidity, resulting in negligible variations in the values of emission quantum yield. The emission color stability was also investigated when these compounds were submitted to long continuous solar irradiation (AM1.5G, 1000 Wm^{-2}), where the red emission persisted unaffected [45]. It is worth mentioning that the red emission of such Eu^{3+} complexes is only perceptible under UV irradiation (300–400 nm) corresponding to a small portion (~6%) of the AM1.5G solar spectrum, resulting in a transparent device under daylight illumination with minor absorption in the visible spectral range(>380 nm)[45-47].

The PMMA/IS-Ln-20 materials exhibited large Stokes-shifts and negligible self-absorption, enabling efficient solar harvesting and conversion (with absorption overlapping the AM1.5G spectrum and complementing that of PV cells), and emission in the red-NIR spectral range which is the region

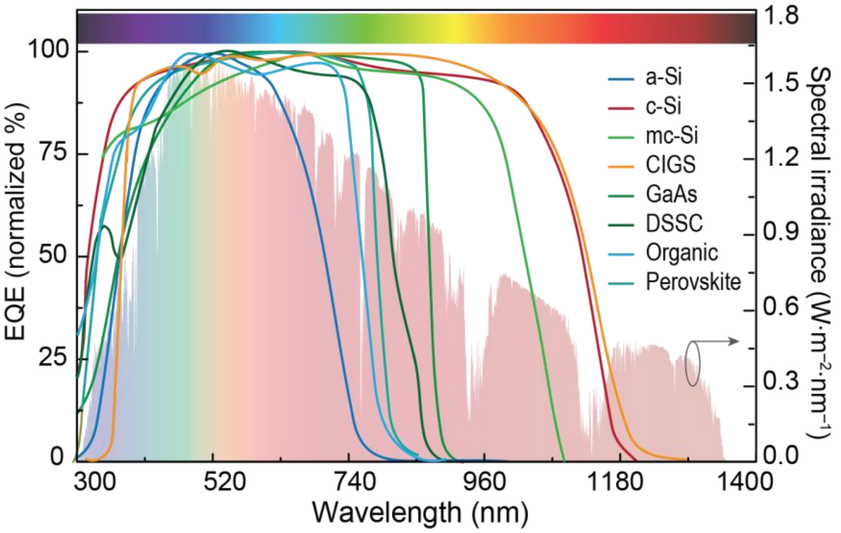

Fig. 1. Normalized external quantum efficiency (EQE) for single-junction PV cells with confirmed terrestrial efficiencies measured under the global AM1.5 spectrum (1000 W·m^{-2}) at a cell temperature of 25 °C, according to [48]. The shadowed area represents the AM1.5G solar spectral irradiance spectrum [34].

where crystalline silicon (c-Si) PV cells demonstrate maximum absorption, (cf. **Fig. 1**, red line). The large molar extinction coefficient and brightness values for the materials resembled those of orange/red emitting organic dyes. Attractive LSCs with optical conversion efficiency values of ~0.27 and ~0.34% were produced with PMMA/IS-Eu-20 and PMMA/IS-Tb-20, respectively [32]. These materials were subsequently tested in a combined configuration where they worked simultaneously as LDS layers and LSCs, by using edge-mounted c-Si PV cells to take advantage of the guided radiation in the LDS layers to increase the electrical output of the system [33]. The significant increase observed in the PV cell absolute external quantum efficiency (~32% between 300-360 nm) relatively to the bare PV cell with an optimized PMMA/IS-Eu-20 coating unequivocally demonstrated the applicability of the novel approach.

Here the structure, morphology, thermal properties, ionic conductivity, and optical features of the family of new electrolytes PMMA/IS-Nd-19/IS-Eu-1/[BMIm][PF$_6$]-X' with a weight ratio IS-Nd:IS-Eu = 19:1 (where [BMIm][PF$_6$] is 1-butyl-3-methylimidazolium hexafluorophosphate ionic liquid (IL), and X' = [BMIm][PF$_6$]/PMMA w/w)) were characterized. We note that the incorporation of the mixture of IS-Nd-19 and IS-Eu-1 ionosilicas into PMMA aimed at ensuring emission in the visible-to-NIR spectral region. The addition of an IL to the electrolyte formulation was encouraged by the unique benefits offered by this sort of compounds, in particular high ionic conductivity, wide electrochemical stability window, low volatility, extended liquid phase temperature range, high thermal stability, non-flammability, and the possibility of structure design by changing the cation and/or anion pair, allowing the tailor of the ILs for a specific application [49]. Besides, most ILs are highly transparent and have been used to substitute lithium salts in the electrolyte since they can perform mutually as mobile ions and plasticizers [50]. In the present case the addition of [BMIm][PF$_6$] was dictated primarily by its hydrophobic nature and thus its ability to dissolve PMMA [51]. The electro-optical performance of the glass/a-IZO/a-WO$_3$/(PMMA/IS-Nd-19/IS-Eu-1/[BMIm][PF$_6$]-55)/c-NiO/a-IZO/glass device, abbreviated as ECD@PISIL (where P is polymer, IS is ionosilica and IL is ionic liquid) (**Fig. 2a**) was investigated. For comparison purposes, the analogue ECD, noted as ECD@IS, in which the electrolyte was exclusively composed of the mixture of IS-Eu and IS-Nd, was also studied.

2 Experimental

2.1 Materials

N-Butylimidazole (BIm, 98%, Sigma-Aldrich), (3-chloropropyl)trimethoxysilane (CPTMS, 97%, Sigma-Aldrich), neodymium(III) chloride

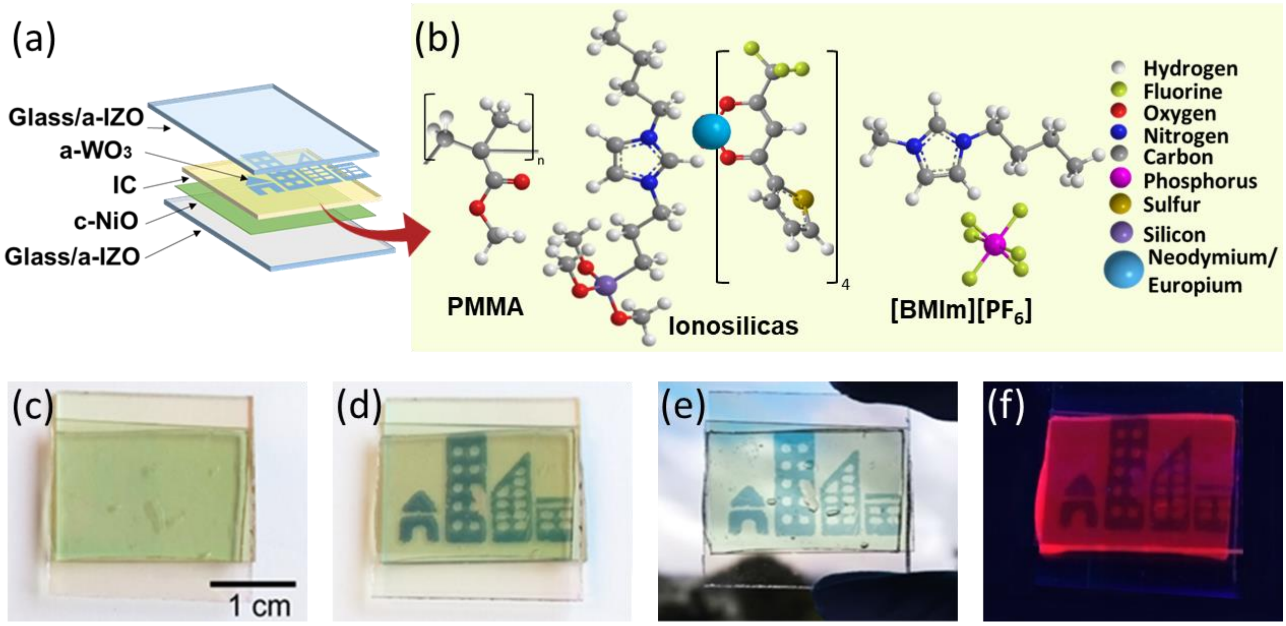

Fig. 2. Archetypal ECD@PISIL featuring the logo of UN Sustainability Goal 11. (a) Schematic representation, where IC is ion conductor; (b) Chemical structures of the components of the optimized IC, i.e., PMMA/IS-Nd-19/IS-Eu-1/[BMIm][PF_6]-55. (c) As-prepared appearance. Colored state at −2.5 V: (d) against a white background; (e) against an outside environment background; (f) under UV radiation (365 nm).

hexahydrate ($NdCl_3.6H_2O$, 99.9%, Sigma-Aldrich), europium(III) chloride hexahydrate ($EuCl_3.6H_2O$, 99.99%, Sigma-Aldrich), 2-thenoyltrifluoroacetone (tta, 99%, Sigma-Aldrich), methyl methacrylate (MM, Sigma-Aldrich), ethanol (EtOH, 99.8%, Fisher Chemical), tetrahydrofuran (THF, Sigma-Aldrich), sodium hydroxide (NaOH, Merck), 1-butyl-3-methylimidazolium hexafluorophosphate ([BMIm][PF_6], 98+%, Alfa Aesar), and anhydrous ethyl acetate (EtOAc, 99.8%, Sigma-Aldrich) were used as received. Ultrapure water was used in all experiments.

2.2 Synthesis of the electrolytes

Synthesis of the IS-Nd-19/IS-Eu-1 mixture. The mixture of ionosilicas, prepared according to the procedure reported elsewhere [32], is briefly described as follows.

1-Butyl-3-[3-(trimethoxysilyl)propyl]imidazolium chloride ([B(TMSP)Im]Cl) was first prepared by mixing BIm with CPTMS (molar ratio BIm:CPTMS = 1:1). The resulting solution was stirred at 70 °C for 5 days under nitrogen atmosphere. The product was washed with anhydrous EtOAc, dried under vacuum, and stored under vacuum conditions.

The synthesis of the Na[Ln$(tta)_4$] compounds with Ln = Nd, Eu involved the dissolution of tta in EtOH, and deprotonation with NaOH (molar ratio tta:NaOH = 4:4) at 50–60 °C for 2 h. An ethanolic solution of $LnCl_3{\cdot}6H_2O$ was subsequently added dropwise (molar ratio tta:NaOH:$LnCl_3{\cdot}6H_2O$ = 4:4:1) and the mixture was kept at 50–60 °C for 1 h. EtOH was then removed, and the as-produced compounds were dried for 3 days at 50 °C.

The preparation of the 1-butyl-3-[3-(trimethoxysilyl)propyl]imidazolium tetra(2-thenoyltrifluoroacetonate) neodymate/europate(III) (III) [B(TMSP)Im][Ln$(tta)_4$] compounds and of the corresponding ionosilicas (IS-Nd-19 and IS-Eu-1) implied mixing Na[Ln$(tta)_4$] with [B(TMSP)Im]Cl in THF under nitrogen atmosphere (molar ratio Na[Ln$(tta)_4$]:[B(TMSP)Im]Cl = 1:1). The resulting sodium chloride (NaCl) was removed by precipitation and centrifugation. The mixture of IS-Nd and IS-Eu ionosilicas (19:1 wt. ratio) was obtained from hydrolysis and condensation of [B(TMSP)Im][Nd$(tta)_4$] and [B(TMSP)Im][Eu$(tta)_4$], respectively (molar ratio [B(TMSP]Im][Ln$(tta)_4$]:EtOH:H_2O=1:4:1.5).

Synthesis of the PMMA/IS-Nd-19/IS-Eu-1/[BMIm][PF_6]-X' electrolytes. A mass of 1 g of MM was first mixed with 0.006 g of benzoyl peroxide in 6 vials. The mixture was heated at 80-90 °C for 25 min. A THF solution of the ionosilica mixture was then added to each vial (20% wt. of IS-Nd-19 plus IS-Eu-1 with respect to MM). The mixture was then doped with [BMIm][PF_6] (X' = 25, 35, 45, 55, 65, and 75 % wt., where X' = m[BMIm][PF_6]/mMM) and subsequently transferred to an oven at 50 °C until complete polymerization. Elemental analysis of PMMA/IS-Nd-19/IS-Eu-1/[BMIm][PF_6]-55. Calculated: Eu, 0.066; Nd, 1.190. Found: Eu, 0.085; Nd, 1.700. The disagreement between the calculated and found values is attributed to MM loss through evaporation (boiling point = 101 ºC) during the synthesis process. We note that the calculated and found Eu:Nd ratio coincided (0.05), as sought.

2.3 Characterization of the electrolytes

Differential Scanning Calorimetry (DSC) measurements were performed with a DSC 204 Netzsch equipment. A mass of 7-10 mg was placed in a 40 µL aluminum pan and stored in a desiccator over P_2O_5 for 1 week at room temperature under vacuum. After the drying treatment, the can was hermetically sealed and the thermogram was recorded. Each electrolyte sample was heated from 20-30 to 300 ºC at 10 ºC min^{-1}. The purge gas was high purity nitrogen supplied at a constant 25 mL min^{-1} flow rate.

X-ray diffraction (XRD) patterns were recorded in the 2θ range spanning from 3 to 50 ° by using a PANalytical Empyrean diffractometer system under exposure of CuKα radiation (1.54 Å) at room temperature. The spacing between planes in the atomic lattice (d) was calculated using Bragg's Law.

The ionic conductivity of the ormolytes was determined by complex impedance measurements. An ormolyte disk was placed between two 10 mm diameter ion blocking gold electrodes (Goodfellow, >99.9 %). The electrode/ormolyte/electrode assembly was secured in a suitable constant-volume support, which was installed in a Buchi TO 51 tube oven. A calibrated type K thermocouple, placed close to the ormolyte disk, was used to measure the sample temperature with a precision of about ±0.2 ºC and samples were characterized over a temperature range of 20-170 ºC. Bulk conductivities of the samples were obtained during heating cycles using the complex plane impedance technique (Autolab PGSTAT-12 (Eco Chemie)) over a frequency range of 65 kHz to 0.5 Hz. The electrolyte behavior was found to be almost ideal and bulk conductivities were extracted in the conventional manner from impedance data by using an equivalent circuit composed of Rb in parallel with Cg, where Rb is the electrical resistance of the electrolyte and Cg is its geometric capacity. The circuit element corresponding to the blocking electrode interface was simulated by a series Cdl element, where Cdl in the double layer capacity.

The Attenuated Total Reflection/Fourier Transform Infrared (ATR/FT-IR) spectra of PMMA, IS-Nd, IS-Eu and PMMA/IS-Nd-19/IS-Eu-1/[BMIm][PF_6]-X' materials were acquired at room temperature in a Bruker Tensor 27 spectrometer equipped with a Specac Golden Gate (Diamond) ATR and the Opus 6.5 software. The spectra were collected in the 4000-350 cm^{-1} range by averaging 256 with at a resolution of 4 cm^{-1}.

The luminescence in the near-infrared (NIR) and in the ultraviolet/visible (UV/VIS) spectral ranges were recorded at room temperature with a modular double grating excitation spectrofluorimeter with a TRIAX 320 emission monochromator (Fluorolog-3, Horiba) coupled to H9170-75 and to R928 Hamamatsu photomultipliers, respectively, using the front face mode. The excitation source was a 450 W Xe arc lamp. The emission spectra were corrected for detection and optical spectral response of the spectrofluorimeter and the excitation spectra were corrected for the spectral distribution of the lamp intensity using a photodiode reference detector.

2.4 Assembly of the ECDs

The configuration adopted for the ECDs included visible and NIR-transparent a-IZO TCO layers, cathodic a-WO_3 as EC1 layer, anodic c-NiO as EC2 layer, and the IC layer sandwiched between them (**Fig. 2(a)**). Upon application of a small voltage, reduction and ion intercalation in a-WO_3, whereas oxidation and ion deintercalation in c-NiO occurred. As a result both electrodes became colored (on state). Bleaching was induced by reversing the voltage (off state).

The a-WO_3 and c-NiO layers were deposited by sputtering and e-beam evaporation, respectively, onto a a-IZO-coated glass previously deposited by sputtering. The a-WO_3 layer was produced in an argon and oxygen atmosphere (oxygen partial pressure of 0.2 Pa) using a deposition pressure of 1.0 Pa, under an r.f. power of 200 W in a Pfeiffer Vacuum Classic 500 system using 3 diameter ceramic target from Plasmaterials, yielding a thickness of 300 nm. A polycrystalline c-NiO film with a 300 nm thickness was obtained from NiO commercial random pellets pieces 3–6 mm (99.99%, Super Conductive Materials), and deposited by e-beam evaporation in a homemade system, with an initial chamber pressure of 7×10^{-4} Pa and growth rate of 6 nm min^{-1}. The a-IZO thin films (resistivity of 7.97×10^{-4} Ω cm, mobility of 52.1 $cm^2 V^{-1} s^{-1}$, and carrier concentration of 1.50 × 1020 cm^{-3}) were deposited by sputtering, in a homemade system, from In_2O_3/ZnO 89.3/10.7 wt%, 99.99%, 3 in. diameter × 6 mm thick (Super Conductive Materials). The sputtering process was carried out at a constant 0.13 Pa value (argon and oxygen) and room temperature. The substrate and target were apart by 10 cm and the r.f. power was 100 W. AFM images of the a-IZO, a-WO_3, and c-NiO layers were recorded in an AFM CSI Nano-Observer equipment (Scientec) in tapping mode using a super sharp Si HQ:NSC19/FORTA probe with a frequency resonance of 60 kHz and a spring constant of 0.3 $N{\cdot}m^{-1}$.

In this work, two ECDs were tested: ECD@PISIL, in which the IC used was the PMMA/IS-Nd-19/IS-Eu-1/[BMIm][PF_6]-55 monolith, and ECD@IS, in which the IC used was the IS-Nd-19/IS-Eu-1 mixture. The prototype ECD@PISIL, with 2.5 × 2 cm^2 active area, was assembled under atmospheric conditions. A piece of the PMMA/IS-Nd-19/IS-Eu-1/[BMIm][PF_6]-55 film with the dimensions of the ECDs and with a thickness of 0.9±0.1 mm was cut out of the monolith and sandwiched between a-WO_3/a-IZO-coated and c-NiO/a-IZO-coated glass plates, so that the two active EC coatings (i.e., a-WO_3 and c-NiO) faced each other. Free space was left on one side of the glass plates to ensure the electrical contacts. The assembled system was then pressed together (**Fig. 2c-2f**) prior to the electro-optical analyses. The ECD@IS prototype, with 2.6 x 1.8 cm^2 active area, was assembled using a similar procedure. The IS-Eu and IS-Nd mixture had to be first heated at 50 °C, prior to being cast onto the surface of the a-WO_3/a-IZO -coated glass with the help of a micropipette.

2.5 Characterization of the ECDs

The optical transmittance (T) of the ECDs was measured in the 400–1650 nm range using a DH Mini, UV-Vis-NIR Lightsource Ocean Optics and a halogen lamp.

Cyclic voltammetry (CV) and chronoamperometry (CA) tests were carried out using a Gamry potentiostat/galvanostat ZRA 11107. In the setup used for measurements the a-WO_3/a-IZO substrate played the role of working electrode, the electrolyte acted as a reservoir of ions for insertion and the c-NiO/a-IZO substrate acted as counter and reference electrodes. The cathodic and anodic charge densities were determined through integration of the CA curves during the coloring and bleaching processes. respectively.

The Commission Internationale d'Éclairage (CIE) 1976 L*a*b* color space ECD coordinates (L* is the lightness (0 = black, 100 = diffuse white), a* is a red–green balance (+a* = red and −a* = green hues), and b* is a yellow–blue balance (+b* = yellow and −b* = blue) were obtained with a Chroma Meter CR-300 Minolta (Osaka, Japan). The L*, a*and b* parameters were calculated from the average values obtained from 3 independent measurements in different places of the window, with a standard deviation below 2%.

3 Results and Discussion

3.1 Structural, thermal and optical characterization of the electrolytes

The ATR/FT-IR spectra of PMMA, IS-Eu, IS-Nd, [BMIm][PF_6], and PMMA/IS-Nd-19/IS-Eu-1/[BMIm][PF_6]-X' samples in the 2000-400 cm^{-1} region are reproduced in **Fig. 3a**. The prominent band produced by PMMA at 1724 cm^{-1} (**Fig. 3a**, black line) is attributed to the stretching vibration of the C=O group, whereas those as 818 and 553 cm^{-1} (**Fig. 3a**, orange line) are associated with the stretching and bending vibration modes of the PF_6^- anion [52], respectively. Analysis of these spectra in the 1760-1680 cm^{-1} interval reveals that in the case of the PMMA/IS-Nd-19/IS-Eu-1/[BMIm][PF_6]-X'

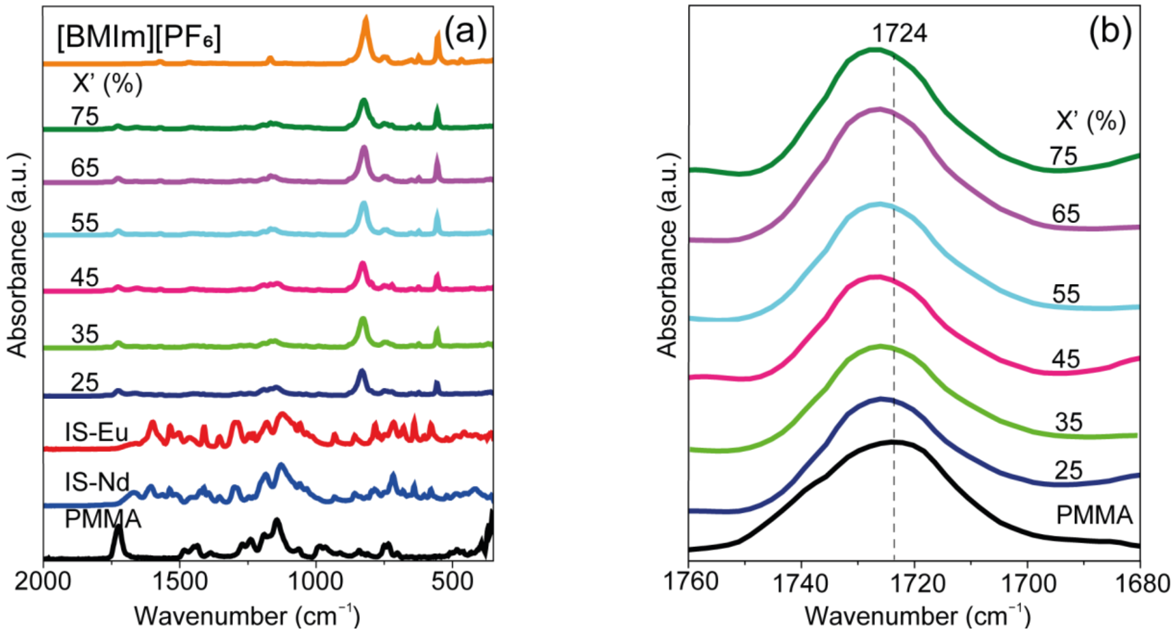

Fig. 3. ATR/FT-IR spectra of PMMA, [BMIm][PF$_6$], IS-Eu, and IS-Nd, and of the PMMA/IS-Nd-19/IS-Eu-1/[BMIm][PF$_6$]-X' electrolytes in the (a) 2000-400 cm^{-1} and (b) 1760-1680 cm^{-1}.

electrolytes (**Fig. 3b**, colored lines) the 1724 cm^{-1} band characteristic of PMMA (**Fig. 3b**, black line) remained essentially unshifted within the spectral resolution of the measurements (*cf.* Experimental section). As to the band profile, it changed slightly upon [BMIm][PF$_6$] addition, demonstrating some band redistribution. These findings suggest that, although the chemical environment around the C=O groups of PMMA may have undergone minor changes after introduction of the IL, globally no substantial bonding between PMMA and [BMIm][PF$_6$] occurred. The same conclusion was reached earlier for PMMA and IS-Ln [33]. Furthermore, inspection of the pair of IL characteristic bands at 818 and 553 cm^{-1} enabled us to confirm that in PMMA/IS-Nd-19/IS-Eu-1/[BMIm][PF$_6$]-X' electrolytes the Ln^{3+} ions do not interact with the PF$_6^-$ anions. Significant superposition of the spectra in critical spectral regions did not allow us drawing any conclusions regarding the interaction between the Ln^{3+} and the [BMIm]$^+$ cations. However, steric hindrance considerations relying on the bulkiness of the tta$^-$ and [BMIm]$^+$ species strongly suggest that Ln^{3+}/[BMIm]$^+$ bonding is extremely unlikely.

The DSC curves of the PMMA/IS-Nd-19/IS-Eu-1/[BMIm][PF$_6$]-X' electrolytes do not exhibit any melting endotherm, confirming the amorphous nature of the materials. The pair of exothermic peaks centered at 161-166 ºC (dominant) and 167-173 ºC (shoulder) are associated with thermal decomposition (onset temperature around 155 °C) (**Fig. 4**) The marked intensity decrease of these two thermal events at increasing [BMIm][PF$_6$] content suggests that the IL exerts a beneficial stabilizing effect on the electrolytes. The latter aspect is particular noteworthy in the sample with X'=75%, for which the peaks practically vanish (**Fig.4**, violet line). In these DSC thermograms it was not possible to detect the glass transition temperature (T$_g$) depression over the whole range of temperatures considered. Scott et al. [53] demonstrated the increasing plasticizing effect exerted by [BMIm][PF$_6$] on the PMMA matrix. An almost linear decrease of T$_g$ with the increase of [BMIm][PF$_6$] concentration between 0-50 wt% was reported (approximately 40 °C at 50 wt% from an initial Tg value around 120 °C). Moreover, Zhao et al. [54] prepared PMMA/MWCNT nanocomposites (where MWCNT stands for multiwalled carbon nanotubes) doped with [BMIm][PF$_6$] and found that this IL was able to reduce drastically the T$_g$ value of the PMMA matrix, thus acting as an efficient plasticizer, and increasing concomitantly the electrical conductivity of the nanocomposites prepared [55].

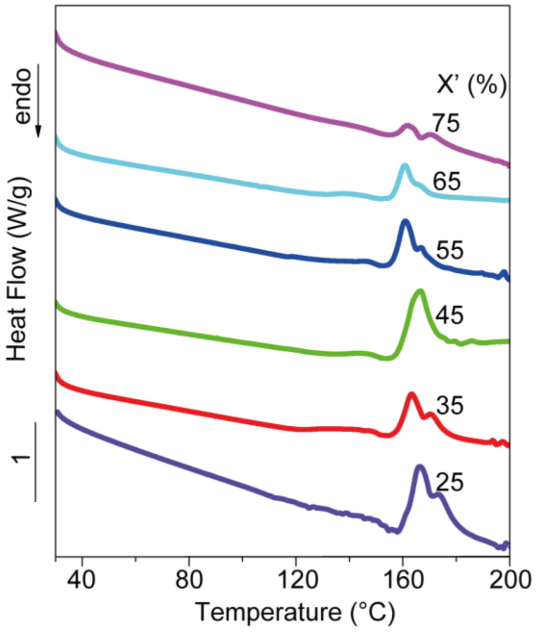

Fig. 4. DSC curves of the PMMA/IS-Nd-19/IS-Eu-1/[BMIm][PF_6]-X' electrolytes.

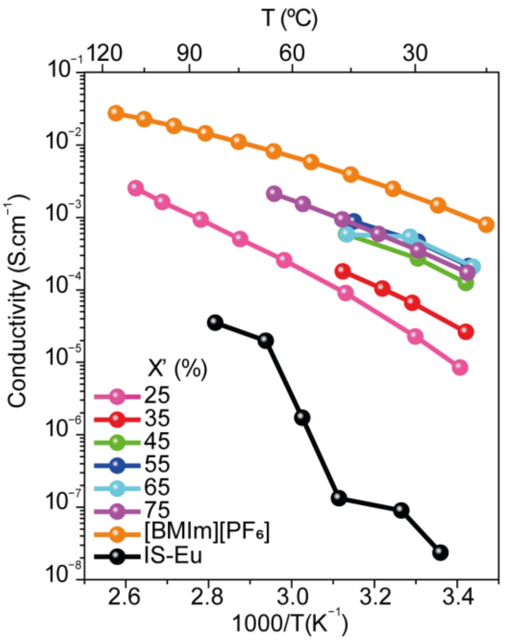

Fig. 5. Temperature dependence of the ionic conductivity of IS-Eu, [BMIm][PF_6] [57] and PMMA/IS-Nd-19/IS-Eu-1/[BMIm][PF_6]-X' electrolytes.

As expected, the ionic conductivity of the doped samples was found to be much higher than that of pure PMMA (ca. 8.57 × 10^{-13} S·cm^{-1} at room temperature [56]) and lower than that of [BMIm][PF_6] (**Fig. 5,** orange line and symbols [57]), reaching its maximum for X' = 55 (**Fig. 5,** blue line and symbols). The temperature dependence of the ionic conductivity of the IL and of the PMMA/IS-Nd-19/IS-Eu-1/[BMIm][PF_6]-X' electrolytes is essentially non-linear, a characteristic trend of amorphous systems that may be described by the Vogel–Tamman–Fulcher (VTF) equation. In the case of IS-Eu an abrupt change around 40-70 °C is detected, which leads to a conductivity increase of about two orders of magnitude (**Fig. 5**, black line and symbols). This dramatic slope change must be associated with the thermal event observed in the DSC curve of IS-Eu in the same temperature interval [33]. The latter event was tentatively attributed to two effects: the order-disorder transition caused by the pendant organic groups placed in the interlamellar space of IS-Eu, and the reversible thermotropic *gauche*/*trans* transition of the butyl group in the imidazolium ring of [BMIm][PF_6] [33]. At last, we note that the ionic conductivity of the PMMA/IS-Nd-19/IS-Eu-1/[BMIm][PF_6]-X' electrolytes is governed by the [BMIm][PF_6] concentration, but the effect is less marked in the most concentrated samples. The sample with X'= 55 was selected for the ECD tests, because it combines high ionic conductivity at lower doping concentration (2.13 × 10^{-4} and 8.76 × 10^{-4} S·cm^{-1} at room temperature and 44 ºC, respectively).

The photoluminescence features of PMMA/IS-Nd-19/IS-Eu-1/[BMIm][PF_6]-55 were examined. This material presents the dual contribution arising from the Eu^{3+} ($^5D_0 \rightarrow {}^7F_{0\text{-}4}$) and Nd^{3+} ($^4F_{3/2} \rightarrow {}^4I_{11/2,13/2}$) intra-4f transitions covering the visible-to-NIR spectral range (**Fig. 6a**). No PMMA intrinsic emission [33] could be observed regardless of the selected excitation wavelength (330-385 nm), indicating efficient PMMA-to-ligand/Ln^{3+} energy transfer [58].

The excitation spectra of PMMA/IS-Nd-19/IS-Eu-1/[BMIm][PF_6]-55 displayed in **Fig. 6b** were monitored selectively for each Ln^{3+} center. The spectrum monitored at the Eu^{3+} emission ($^5D_0 \rightarrow {}^7F_2$ transition) shows two main components peaking at 330 and 385 nm. The low intensity of the intra-$4f^6$ lines indicates that the Eu^{3+} excited states in PMMA are populated via ligand-sensitization. The 330 and 385 nm components resemble those already observed for isolated $Eu(tta)_3(H_2O)_2$ [59] and for organic-inorganic hybrids incorporating $Eu(tta)_3(H_2O)_2$ and $Eu(tta)_3(phen)$ (where phen is 1,10-phenantroline), being ascribed to the π–π*

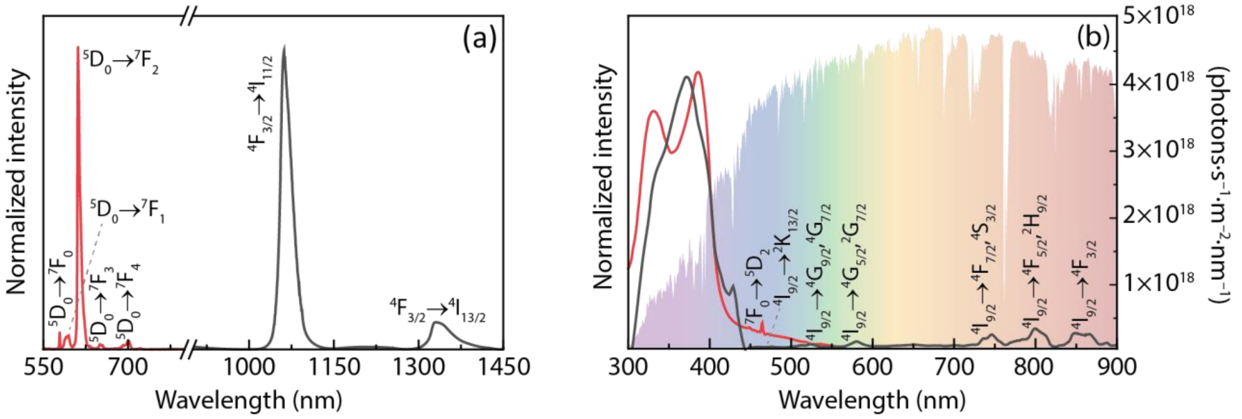

Fig. 6. Emission spectra excited at 360 nm (a) and excitation spectra monitored at 612 nm (red line) and 1056 nm (black line) (b) for PMMA/IS-Nd-19/IS-Eu-1/[BMIm][PF$_6$]-55. The shadowed area represents the AM1.5G photon flux (right *y* axis).)

electronic transition of the organic ligands [51]. In the case of the spectrum monitored at the Nd^{3+} emission ($^4F_{3/2} \rightarrow {}^4I_{11/2}$ transition), the ligands band is also present (despite changes in the relative intensity) overlapping the characteristic transitions of Nd^{3+}. We note that the material is transparent, absorbing mainly the UV component of the sunlight, as illustrated in **Fig. 6b**. The ECD@PISIL exhibits red emission when exposed to UV light (365 nm) (**Fig. 2f**).

The knowledge of solar radiation durability of solar exposed materials is known to be fundamental in the case of LDS layers, LSCs, and ECDs whose formulation usually includes polymers, a family of materials particularly vulnerable to exposure to solar radiation. In the case of PMMA, the polymer used in the present work, photodegradation is predominantly caused by UV radiation with wavelengths shorter than 320 nm [60]. The process is initiated with radicalization of the ester side group leading to β-scission of the polymer backbone and decomposition of the radical end. Creep, dimensional instability, and yellowing are the most common manifestations of photodegradation. Additives, such as UV absorbers, hindered amine light stabilizers, and radical scavengers, are usually included in polymer formulations to supress the latter effect [61]. The absorption features of PMMA/IS-Nd-19/IS-Eu-1/[BMIm][PF$_6$]-55 described above substantiate that the incorporation of the [Nd(tta)$_4$]$^-$ and [Eu(tta)$_4$]$^-$ anions into PMMA has a further benefit. As the tta$^-$ ligand absorbs in the UV region of the solar spectrum, PMMA yellowing is avoided.

3.2 Electro-optical performance of the ECDs

As-prepared ECD@PISIL (**Fig. 2c**) exhibited T values of ca. 79, 96, 89 and 77 % at 555, 1000, 1500 and 1650 nm, respectively (**Table 1** and **Fig. 7a)**, red line) and a light greenish hue (L* = 59.66, a* = −4.62 and b* = 2.46) (**Fig. 8a)**, white circle). The absorption peaks observed from 500 to 800 nm in the visible-NIR spectra reproduced in **Fig. 7a** are associated with the energy levels of Nd^{3+} ion.

The ECD@PISIL was subject to three series of cycling procedures. The 1st cycling series comprised the application of: (1) 10 CV cycles (±1.0 V, 50 mV/s) followed by a CA cycle (0.0 V, 200 s; − 1.0 V, 200 s; +1.0 V, 200 s), (2) 10 CV cycles (±1.5 V, 50 mV/s) followed by a CA cycle (0.0 V, 200 s; − 1.5 V, 200 s; +1.5 V, 200 s), (3) 10 CV cycles (±2.0 V, 50 mV/s) followed by a CA cycle (0.0 V, 200 s; − 2.0 V, 200 s; 2.0 V, 200 s), (4) 10 CV cycles (±2.5 V, 50 mV/s). The T values were then recorded for +2.5/−2.5 V, being 44/34 %, 46/32 %, 39/26 % and 27/13 % at 555, 1000, 1500 and 1650 nm, respectively (**Fig. 7a**, light blue/dark blue lines, and **Table 1**). **Figs. 2d** and **2e** show the colored ECD@PISIL against a white background, and as a window frame, respectively. The 2nd cycling series included 1 CA cycle (0.0 V, 200 s; − 2.5 V, 200 s; 2.5V, 200 s), 2 CA cycles (±3.0 V, 200 s), 12 CA cycles (±2.5 V, 50 s) and 4 CA (±2.5 V, 30 s). At last, cycling series 3 involved 200 CA cycles (±2.5 V, 50 s). As a result, a decline in the T values to 28, 26, 20 and 9 % at 555, 1000, 1500 and 1650 nm,

Table 1. Electro-optical parameters of ECD@ PISIL and ECD@IS. T values are given in %. ΔT is the optical contrast (ΔT = $T_{\text{bleached}}-T_{\text{colored}}$ at a given wavelength).

	λ	$T_{\text{as-prepared}}$	T_{bleached}[a]	T_{colored}[a]	ΔT[a]	ΔOD[a]	T_{bleached}[b]	T_{colored}[b]	ΔT[b]	ΔOD[b]	CE_{in}[b]	CE_{out}[b]
	[nm]	0.0 V	2.5 V	−2.5 V			2.5 V	−2.5 V			($cm^2\ C^{-1}$)	
ECD@PISIL	555	79	44	34	10	0.11	44	28	16	0.20	−302	181
	1000	96	46	32	14	0.16	46	26	20	0.25	−381	228
	1500	89	39	26	13	0.18	39	20	19	0.29	−446	267
	1650	77	27	13	14	0.32	27	9	18	0.48	−734	440
		0.0 V	2.0 V	−2.0V			2.0 V	−2.0 V				
ECD@IS	555	75	69	67	2	0.01	44	41	3	0.03	-201	152
	1000	83	68	67	1	0.01	36	34	2	0.02	-162	123
	1500	80	63	62	2	0.01	32	31	1	0.01	-90	68
	1650	76	61	59	2	0.01	29	28	1	0.01	-100	75

[a] After 1st series of cycling. See text for details.

[b] After 3rd series of cycling (200 CA cycles/50 CA cycles)

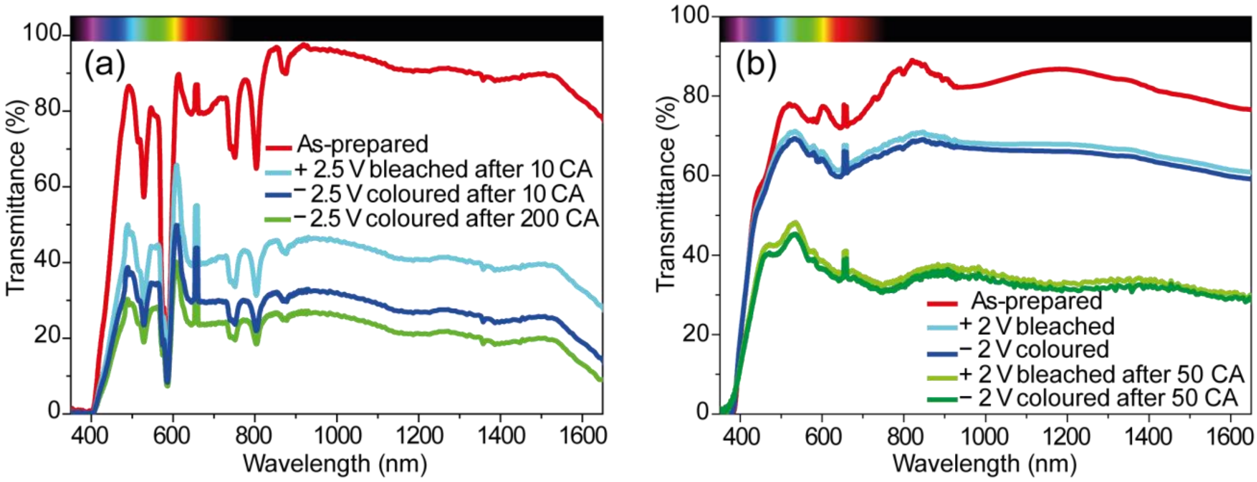

Fig. 7. Visible-NIR spectra of the ECDs: (a) ECD@PISIL in the as-prepared state (red line), bleached state (light blue line), and colored states (dark blue and green lines). (b) ECD@IS in the as-prepared state (red line), bleached states (light blue and light green lines) and colored states (dark blue and dark green lines).

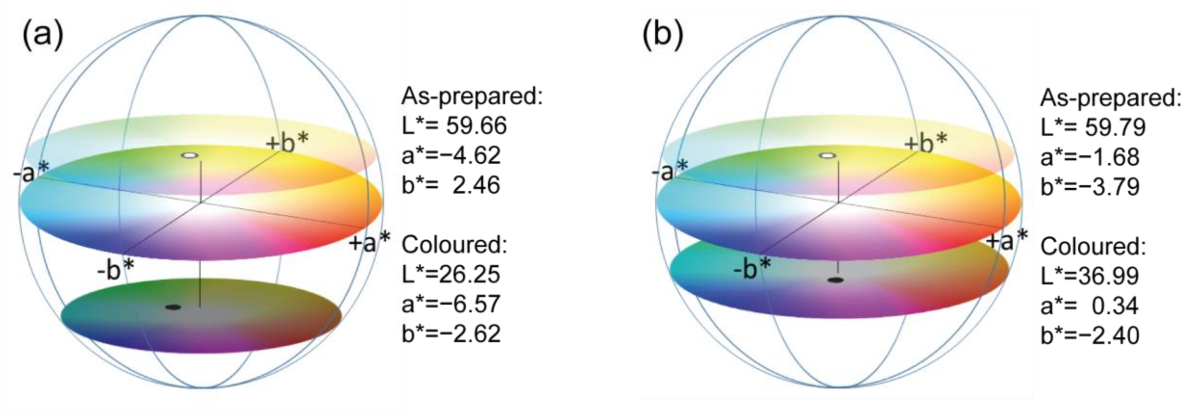

Fig. 8. CIE 1976 L*a*b* color diagram of the ECDs. (a) ECD@PISIL: as-deposited state (white circle), and colored state at −2.5 V after 200 CA cycles (black circle). (b) ECD@IS: as-deposited state (white circle), colored state at −2.0 V after 50 CA cycles (black circle).

respectively, occurred (**Fig. 7a**, green line, and **Table 1**).

The study of the ECD@PISIL over 200 bleaching/coloring CA cycles (±2.5 V at every 50 s) (**Fig. 9a**) demonstrated the excellent cycling stability of the device. As expected, after this CA treatment the T values for the colored state decreased considerably with respect to those measured in the first cycles (**Table 1**). Accordingly, the optical density (ΔOD) (where $\Delta OD = -\log(T_{colored}/T_{bleached})$) values were markedly enhanced (**Table 1**). The CE_{in}/CE_{out} values (where CE, coloration efficiency, measures the change in optical density acquired by injection of charge per unit area, i.e., $CE = \Delta OD/\Delta Q$, Q being the inserted/desinserted charge density) calculated at the 200th cycle at 555, 1000, 1500 and 1650 nm were −302/+181, −381/+228, −446/+267, and −734/+440 $cm^2\ C^{-1}$ for coloration/bleaching, respectively. These CE values are considerably lower than those obtained with the analogue a-IZO-based ECD containing the sol-gel derived $DUPIL_{60}$ electrolyte (−12538/+2901 $cm^2\ C^{-1}$ at 555 nm) [19], but are significantly higher than those reported for an indium tin oxide (ITO)-based analogue ECD incorporating the sol-gel derived poly(ε-caprolactone) (PCL(530))/siloxane di-urethanesil hybrid doped with potassium triflate and the $Eu(btfac)_3phen$ complex (where $btfac^-$ is 4,4,4-trifluoro-1-phenyl-2,4-butanedionate), for which a CE_{in} value of −126 $cm^2\ C^{-1}$ in the visible spectral region was calculated [62]. The most striking aspect of **Fig. 9** is the huge difference between the cathodic and anodic current densities. This result is corroborated by the fact that the T values of the bleached state (**Fig. 7a)**, light blue line) did not coincide with that of the as-prepared state (**Fig. 7a**, red line). The same situation, although less marked, was detected in the $DUPIL_{60}$-based ECD including the same TCO material (a-IZO) and the same active electrodes (a-WO_3 and c-NiO) [19]. This effect was associated with the structure/morphology of the a-IZO, a-WO_3 and c-NiO layers. The first two materials are amorphous and displayed low average roughness values, whereas c-NiO is polycrystalline and exhibited a less homogenous surface topography. As a consequence, the cathodic process was facilitated over the anodic process, and thus less charge was needed to trigger the optical effect (coloration). In the case of ECD@PISIL, it appears that the bulky character of the complex anion of the electrolyte further slowed down the disinsertion process.

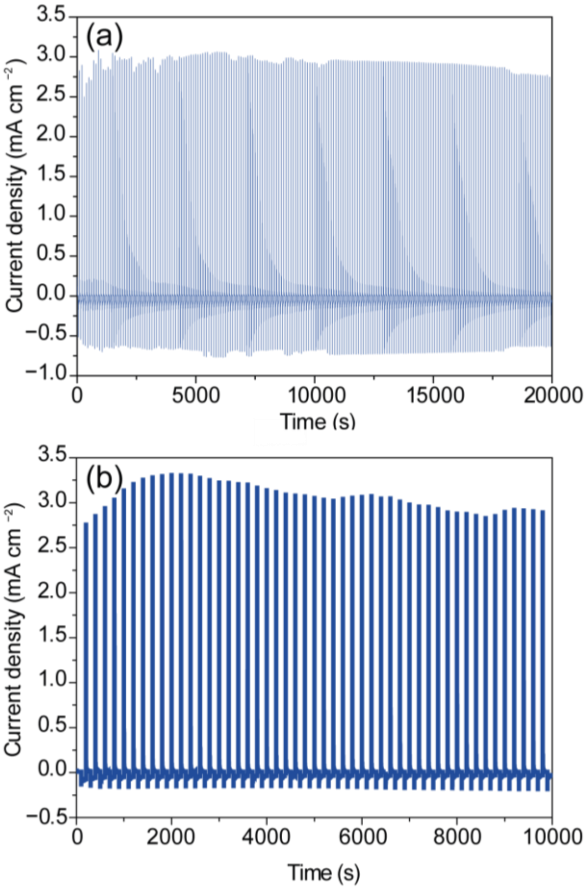

Fig. 9. Variation of the current density of the devices: (a) ECD@PISIL after 200 cycles at voltage steps of ±2.5 V at every 50 s. (b) ECD@IS after 50 cycles at voltage steps of ±2.0 V at every 100 s.

For comparison purposes, the ECD@IS was also tested. The as-prepared device, lacking both PMMA and $[BMIm][PF_6]$, exhibited T values of 75, 83, 80 and 76% at 555, 1000, 1500 and 1650 nm, respectively (**Table 1**, and **Fig. 7b**, red line), and a light blueish hue (L* = 59.79, a* = −1.68 and b* = −3.79) (**Fig. 8b**, white circle). The ECD@IS was first subject to 10 CA cycles (±2.0 V, 100 s). As a consequence, the T values recorded for the bleached (**Fig. 7b**, light blue) and colored (**Fig. 7b**, dark blue) states decreased. When the ECD@IS was subsequently submitted to 50 CA cycles (±2.0 V, 100 s) (**Fig. 7b**), the T values of the bleached/colored states dropped to 44/41%, 36/34%, 32/31% and 29/28% at 555, 1000, 1500 and 1650 nm, respectively (**Table 1**, and **Fig. 7b**, light green/dark green lines), and a dark blue color (L* =

36.99, a* = 0.34 and b* = −2.40) (**Figs. 8b**, black circle) resulted. **Fig. 9b** illustrates again the dramatic difference in terms of current density required for charge and discharge. The calculated ΔOD values are rather small (**Table 1**). The CE_{in}/CE_{out} values calculated at the 50th cycle at 555, 1000, 1500 and 1650 nm were −201/+152, −162/+123, −90/+68, and −100/+75 cm^2 C^{-1} for coloration/bleaching, respectively (**Table 1**), thus markedly lower than those observed for ECD@PISIL. The poorer electro-optical performance of ECD@IS demonstrates the beneficial effect resulting from the use of an electrolyte sample with higher conductivity (**Fig. 4**).

Conclusions

A red-emitting glass/a-IZO/a-WO_3/(PMMA/IS-Nd-19/IS-Eu-1/[BMIm][PF_6]-55)/c-NiO/a-IZO/glass ECD device, noted as ECD@PISIL, enabling simultaneous control of the transmission of the visible and NIR solar radiation hitting the device, was produced. The encouraging performance of the device represents the proof-of-concept that confirms that the luminescent film PMMA/IS-Nd-19/IS-Eu-1/[BMIm][PF_6]-55, which was used previously (with a formulation lacking the IL) in a combined configuration where it worked simultaneously as LSC and LDS layers [33], can also act as electrolyte of an ECD. Further studies devoted to the improvement of this ECD are clearly justified aiming the development of integrated harvesting/conversion/management LSC-LDS/PV/ECD systems. Given the impressive figures of merit of the ECD including $DUPIL_{60}$, an electrolyte composed of the di-ureasil d-U(2000) and [BIm][TfO] PIL [19], changing [BMIm][PF_6] by a PIL in which PMMA is soluble will be the natural first choice to try. The synthesis via sol-gel chemistry of other host matrices through the co-condensation of appropriate precursors, such as 3-(trimethoxysilyl)propyl methacrylate (TMSPMA) and/or di-urea cross-linked propyltriethoxysilane (d-UPTES(2000) [19]) with [B(TMSP)Im][Ln$(tta)_4$] [32] appears also very attractive. This approach could be obviously extended to other organic/inorganic hybrids able to impart simultaneously transparency and flexibility.

Acknowledgment This work was supported by National Funds by FCT –Foundation for Science and Technology and, whenever applicable, by FEDER funds through the POCI – COMPETE 2020 – Operational Programme Competitiveness and Internationalization in Axis I – Strengthening research, technological development and innovation (UIDB/00616/2020, UIDP/00616/2020, UID/QUI/00686/2020, UID/QUI/00313/2020, UIDB/50006/2020, SOLPOWINS-PTDC/CTM-REF/4304/2020, OBTAIN-NORTE-01-0145-FEDER-000084, and PTDC/BTM-MAT/30858/2017). This work was also developed within the scope of the project CICECO-Aveiro Institute of Materials, UIDB/50011/2020 & UIDP/50011/2020, financed by Portuguese funds through the FCT/MCTES. M.A. Cardoso acknowledges FCT for the PhD grant SFRH/BD/118466/2016 and S.F.H. Correia acknowledges SolarFlex (CENTRO-01–0145-FEDER-030186).

Compliance with ethical standards

Conflict of interest The authors declare no competing interests.

References

1. Energy performance of buildings directive. In: Eur. Comm. https://ec.europa.eu/energy/topics/energy-efficiency/energy-efficient-buildings/energy-performance-buildings-directive_en. Accessed 19 Apr 2021
2. Granqvist CG, Arvizu MA, Pehlivan IB, Qu HY, Wen RT, Niklasson GA (2018) Electrochromic materials and devices for energy efficiency and human comfort in buildings: A critical review. Electrochim Acta 259:1170–1182. https://doi.org/10.1016/j.electacta.2017.11.169
3. Nearly zero-energy buildings. In: Eur. Comm. https://ec.europa.eu/energy/en/topics/energy-efficiency/buildings/nearly-zero-energy-buildings. Accessed 19 Apr 2021
4. Renewable energy directive. In: Eur. Comm. https://ec.europa.eu/energy/topics/renewable-energy/renewable-energy-directive_pt. Accessed 19 Apr 2021
5. Energy efficiency. In: Eur. Comm. https://ec.europa.eu/energy/topics/energy-efficiency_en. Accessed 19 Apr 2021
6. Energy efficiency directive. In: Eur. Comm. https://ec.europa.eu/energy/topics/energy-efficiency/targets-directive-and-rules/energy-efficiency-directive_en. Accessed 19 Apr 2021
7. 2030 climate & energy framework. In: Eur. Comm. https://ec.europa.eu/clima/policies/strategies/2030_en. Accessed 19 Apr 2021

8. 2050 long-term strategy. In: Eur. Comm. https://ec.europa.eu/clima/policies/strategies/2050_en. Accessed 19 Apr 2021
9. A European Green Deal. In: Eur. Comm. https://ec.europa.eu/info/strategy/priorities-2019-2024/european-green-deal_en. Accessed 19 Apr 2021
10. United Nations Take Action for the Sustainable Development Goals. https://www.un.org/sustainabledevelopment/sustainable-development-goals/. Accessed 19 Apr 2021
11. Guterres A (2020) Remarks to International Energy Agency Clean Energy Transition Summit. In: United Nations Secr. https://www.un.org/sg/en/content/sg/speeches/2020-07-09/remarks-international-energy-agency-clean-energy-transition-summit. Accessed 19 Apr 2021
12. Casini M (2018) Active dynamic windows for buildings: A review. Renew Energy 119:923–934. https://doi.org/10.1016/j.renene.2017.12.049
13. DeForest N, Shehabi A, O'Donnell J, Garcia G, Greenblatt J, Lee ES, Selkowitz S, Milliron DJ (2015) United States energy and CO2savings potential from deployment of near-infrared electrochromic window glazings. Build Environ 89:107–117. https://doi.org/10.1016/j.buildenv.2015.02.021
14. Llordés A, Garcia G, Gazquez J, Milliron DJ (2013) Tunable near-infrared and visible-light transmittance in nanocrystal-in-glass composites. Nature 500:323–326. https://doi.org/10.1038/nature12398
15. Kim J, Ong GK, Wang Y, LeBlanc G, Williams TE, Mattox TM, Helms BA, Milliron DJ (2015) Nanocomposite Architecture for Rapid, Spectrally-Selective Electrochromic Modulation of Solar Transmittance. Nano Lett 15:5574–5579. https://doi.org/10.1021/acs.nanolett.5b02197
16. Xu J, Zhang Y, Zhai TT, Kuang Z, Li J, Wang Y, Gao Z, Song YY, Xia XH (2018) Electrochromic-Tuned Plasmonics for Photothermal Sterile Window. ACS Nano 12:6895–6903. https://doi.org/10.1021/acsnano.8b02292
17. Zhang S, Cao S, Zhang T, Fisher A, Lee JY (2018) Al 3+ intercalation/de-intercalation-enabled dual-band electrochromic smart windows with a high optical modulation, quick response and long cycle life. Energy Environ Sci 11:2884–2892. https://doi.org/10.1039/c8ee01718b
18. Barawi M, Veramonti G, Epifani M, Giannuzzi R, Sibillano T, Giannini C, Rougier A, Manca M (2018) A dual band electrochromic device switchable across four distinct optical modes. J Mater Chem A 6:10201–10205. https://doi.org/10.1039/c8ta02636j
19. Cardoso MA, Pereira RFP, Pereira S, Gonçalves H, Silva MM, Carlos LD, Nunes SC, Fortunato E, Ferreira RAS, Rego R, Bermudez VZ (2019) Micro-Thermoelectric Devices: Three-Mode Modulation Electrochromic Device with High Energy Efficiency for Windows of Buildings Located in Continental Climatic Regions. Adv Sustain Syst 3:1970007. https://doi.org/10.1002/adsu.201970007
20. Gonçalves HMR, Pereira RFP, Lepleux E, Carlier T, Pacheco L, Pereira S, Valente AJM, Fortunato E, Duarte AJ, Bermudez VZ (2019) Nanofluid Based on Glucose-Derived Carbon Dots Functionalized with [Bmim]Cl for the Next Generation of Smart Windows. Adv Sustain Syst 3:1900047. https://doi.org/10.1002/adsu.201900047
21. Nunes SC, Saraiva SM, Pereira RFP, Pereira S, Silva MM, Carlos LD, Fortunato E, Ferreira RAS, Rego R, Bermudez VZ (2019) Sustainable Dual-Mode Smart Windows for Energy-Efficient Buildings. ACS Appl Energy Mater 2:1951–1960. https://doi.org/10.1021/acsaem.8b02041
22. Gonçalves MC, Pereira RFP, Alves R, Nunes SC, Fernandes M, Gonçalves HMR, Pereira S, Silva MM, Fortunato E, Rego R, Bermudez VZ (2020) Electrochromic Device Composed of a Di-Urethanesil Electrolyte Incorporating Lithium Triflate and 1-Butyl-3-Methylimidazolium Chloride. Front Mater 7:. https://doi.org/10.3389/fmats.2020.00139
23. Baetens R, Jelle BP, Gustavsen A (2010) Properties, requirements and possibilities of smart windows for dynamic daylight and solar energy control in buildings: A state-of-the-art review. Sol Energy Mater Sol Cells 94:87–105. https://doi.org/10.1016/j.solmat.2009.08.021
24. Jelle BP, Hynd A, Gustavsen A, Arasteh D, Goudey H, Hart R (2012) Fenestration of today and tomorrow: A state-of-the-art review and future research opportunities. Sol Energy Mater Sol Cells 96:1–28. https://doi.org/10.1016/j.solmat.2011.08.010
25. Fernandes M, de Zea Bermudez V (2021) Sol-gel materials for smart electrochromic devices. In: Chemical Solution Synthesis for Materials Design and Thin Film Device Applications, Soumen Das. Elsevier, pp 439–475
26. Mortimer RJ, Rosseinsky DR, Monk PMS (2013) Electrochromic Materials and Devices. Wiley-VCH Verlag GmbH & Co. KGaA, Weinheim, Germany
27. Piccolo A, Simone F (2015) Performance requirements for electrochromic smart window. J Build Eng 3:94–103. https://doi.org/10.1016/j.jobe.2015.07.002
28. Fernandes M, Freitas V, Pereira S, Leones R, Silva MM, Carlos LD, Fortunato E, Ferreira RAS, Rego R, Bermudez VZ (2018) Luminescent Electrochromic Devices for Smart Windows of Energy-Efficient Buildings. Energies 11:3513. https://doi.org/10.3390/en11123513
29. Barquinha P, Gonçalves G, Pereira L, Martins R, Fortunato E (2007) Effect of annealing temperature on the properties of IZO films and IZO based transparent TFTs. Thin Solid Films 515:8450–8454. https://doi.org/10.1016/j.tsf.2007.03.176
30. Davy NC, Sezen-Edmonds M, Gao J, Lin X, Liu A, Yao N, Kahn A, Loo Y-L (2017) Pairing of near-ultraviolet solar cells with electrochromic windows for smart management of the solar spectrum. Nat Energy 2:17104. https://doi.org/10.1038/nenergy.2017.104
31. Jelle BP, Breivik C (2012) State-of-the-art Building Integrated Photovoltaics. Energy Procedia 20:68–77. https://doi.org/10.1016/j.egypro.2012.03.009
32. Frias A, Cardoso M, Bastos A, Correia SFH, André PS, Carlos LD, Bermudez VZ, Ferreira RAS (2019) Transparent Luminescent Solar Concentrators Using Ln^{3+}-Based Ionosilicas Towards Photovoltaic Windows. Energies 12:451. https://doi.org/10.3390/en12030451
33. Cardoso MA, Correia SFH, Frias AR, et al (2020) Solar spectral conversion based on plastic films of lanthanide-doped ionosilicas for photovoltaics: Down-shifting layers

and luminescent solar concentrators. J Rare Earths 38:531–538. https://doi.org/10.1016/j.jre.2020.01.007

34. Ferreira RAS, Correia SFH, Monguzzi A, Liu X, Meinardi F (2020) Spectral converters for photovoltaics – What’s ahead. Mater Today 33:105–121. https://doi.org/10.1016/j.mattod.2019.10.002
35. Klampaftis E, Ross D, McIntosh KR, Richards BS (2009) Enhancing the performance of solar cells via luminescent down-shifting of the incident spectrum: A review. Sol Energy Mater Sol Cells 93:1182–1194. https://doi.org/10.1016/j.solmat.2009.02.020
36. Hovel HJ, Hodgson RT, Woodal JM (1979) The effect of fluorescent wavelength shifting on solar cell spectral response. Sol Energy Mater 2:19–29. https://doi.org/10.1016/0165-1633(79)90027-3
37. Strümpel C, McCann M, Beaucarne G, Arkhipov V, Slaoui A, Švrček V, del Cañizo C, Tobias I (2007) Modifying the solar spectrum to enhance silicon solar cell efficiency—An overview of available materials. Sol Energy Mater Sol Cells 91:238–249. https://doi.org/10.1016/j.solmat.2006.09.003
38. McIntosh KR, Lau G, Cotsell JN, Hanton K, Bätzner DL, Bettiol F, Richards BS (2009) Increase in external quantum efficiency of encapsulated silicon solar cells from a luminescent down-shifting layer. Prog Photovoltaics Res Appl 17:191–197. https://doi.org/10.1002/pip.867
39. Rothemund R, Kreuzer S, Umundum T, Meinhardt G, Fromherz T, Jantsch W (2011) External quantum efficiency analysis of Si solar cells with II-VI nanocrystal luminescent down-shifting layers. Energy Procedia 10:83–87. https://doi.org/10.1016/j.egypro.2011.10.157
40. Farinhas J, Correia SFH, Fu L, Botas AMP, André PS, Ferreira RAS, Charas A (2021) Ultraviolet-Filtering Luminescent Transparent Coatings for High-Performance PTB7-Th:ITIC–Based Organic Solar Cells. Front Nanotechnol 3:. https://doi.org/10.3389/fnano.2021.635929
41. Thakur VK, Ding G, Ma J, Lee PS, Lu X (2012) Hybrid materials and polymer electrolytes for electrochromic device applications. Adv Mater 24:4071–4096. https://doi.org/10.1002/adma.201200213
42. Kai JA, Felinto MCFC, Nunes LAO, Malta OL, Brito HF (2011) Intermolecular energy transfer and photostability of luminescence-tuneable multicolour PMMA films doped with lanthanide-beta-diketonate complexes. J Mater Chem 21:3796–3802. https://doi.org/10.1039/C0jm03474f
43. Lima PP, Ferreira RAS, Freire RO, Paz FAA, Fu L, Alves S, Carlos LD, Malta OL (2006) Spectroscopic Study of a UV-Photostable Organic-Inorganic Hybrids Incorporating an Eu3+ β-Diketonate Complex. ChemPhysChem 7:735–746. https://doi.org/10.1002/cphc.200500588
44. Lima PP, Nolasco MM, Paz FAA, Ferreira RAS, Longo RL, Malta OL, Carlos LD (2013) Photo–Click Chemistry to Design Highly Efficient Lanthanide β-Diketonate Complexes Stable under UV Irradiation. Chem Mater 25:586–598. https://doi.org/10.1021/cm303776x
45. Ramalho JFCB, Correia SFH, Fu L, Dias LMS, Adão P, Mateus P, Ferreira RAS, André PS (2020) Super modules-based active QR codes for smart trackability and IoT: a responsive-banknotes case study. npj Flex Electron 4:11. https://doi.org/10.1038/s41528-020-0073-1
46. Correia SFH, Frias AR, Fu L, Rondão R, Pecoraro E, Ribeiro SJL, André PS, Ferreira RAS, Carlos LD (2018) Large-Area Tunable Visible-to-Near-Infrared Luminescent Solar Concentrators. Adv Sustain Syst 2:1800002. https://doi.org/10.1002/adsu.201800002
47. Correia SFH, Bastos ARN, Fu L, Carlos LD, André PS, Ferreira RAS (2019) Lanthanide-based downshifting layers tested in a solar car race. Opto-Electronic Adv 2:19000601–19000608. https://doi.org/10.29026/oea.2019.190006
48. Green MA, Dunlop ED, Levi DH, Hohl-Ebinger J, Yoshita M, Ho-Baillie AWY (2019) Solar cell efficiency tables (version 54). Prog Photovoltaics Res Appl 27:565–575. https://doi.org/10.1002/pip.3171
49. Lunstroot K, Driesen K, Nockemann P, Görller-Walrand C, Binnemans K, Bellayer S, Le Bideau J, Vioux A (2006) Luminescent ionogels based on europium-doped ionic liquids confined within silica-derived networks. Chem Mater 18:5711–5715. https://doi.org/10.1021/cm061704w
50. Tang Q, Li H, Yue Y, Zhang Q, Wang H, Li Y, Chen P (2017) 1-Ethyl-3-methylimidazolium tetrafluoroborate-doped high ionic conductivity gel electrolytes with reduced anodic reaction potentials for electrochromic devices. Mater Des 118:279–285. https://doi.org/10.1016/j.matdes.2017.01.033
51. Ali U, Karim KJBA, Buang NA (2015) A Review of the Properties and Applications of Poly (Methyl Methacrylate) (PMMA). Polym Rev 55:678–705. https://doi.org/10.1080/15583724.2015.1031377
52. Logacheva NM, Baulin VE, Tsivadze AY, Pyatova EN, Ivanova IS, Velikodnyc YA, Chernyshev VV (2009) Ni(II), Co(II), Cu(II), Zn(II) and Na(I) complexes of a hybrid ligand 4′-(4‴-benzo-15-crown-5)-methyloxy-2,2′:6′,2″-terpyridine. Dalton Trans 2482–2489. https://doi.org/10.1039/b819805e
53. Scott MP, Brazel CS, Benton MG, Mays JW, Holbrey JD, Rogers RD (2002) Application of ionic liquids as plasticizers for poly(methyl methacrylate). Chem Commun 2:1370–1371. https://doi.org/10.1039/b204316p
54. Zhao L, Li Y, Cao X, You J, Dong W (2012) Multifunctional role of an ionic liquid in melt-blended poly(methyl methacrylate)/ multi-walled carbon nanotube nanocomposites. Nanotechnology 23:255702. https://doi.org/10.1088/0957-4484/23/25/255702
55. Shamsuri AA, Daik R (2015) Applications of ionic liquids and their mixtures for preparation of advanced polymer blends and composites: A short review. Rev Adv Mater Sci 40:45–59
56. Othman L, Chew KW, Osman Z (2007) Impedance spectroscopy studies of poly (methyl methacrylate)-lithium salts polymer electrolyte systems. Ionics 337–342. https://doi.org/10.1007/s11581-007-0120-0
57. Zech O, Stoppa A, Buchner R, Kunz W (2010) The Conductivity of Imidazolium-Based Ionic Liquids from (248 to 468) K. B. Variation of the Anion. J Chem Eng Data 55:1774–1778. https://doi.org/10.1021/je900793r
58. Fernandes M, de Zea Bermudez V, Ferreira RAS, Carlos LD, Charas A, Morgado J, Silva MM, Smith MJ (2007) Highly Photostable Luminescent Poly (E-caprolactone) siloxane Biohybrids Doped with Europium Complexes. Chem Mater 19:3892–3901. https://doi.org/10.1021/cm062832n

59. Fernandes M, de Zea Bermudez V, Ferreira RAS, Carlos LD, Martins NV (2008) Incorporation of the Eu(tta)3(H2O)2 complex into a co-condensed d-U(600)/d-U(900) matrix. J Lumin 128:205–212. https://doi.org/10.1016/j.jlumin.2007.07.009
60. Murray MP, Bruckman LS, French RH (2012) Photodegradation in a stress and response framework: poly(methyl methacrylate) for solar mirrors and lens. J Photonics Energy 2:022004. https://doi.org/10.1117/1.JPE.2.022004 and references therein
61. Poliskie M (2016) Solar Module Packaging. CRC Press, Boca Raton
62. Fernandes M, Botas AMP, Leones R, Pereira S, Silva MM, Ferreira RAS, Carlos LD, Fortunato E, Rego E, Bermudez VZ (2014) Luminescent Electrochromic Device Based on a Biohybrid Electrolyte Doped with a Mixture of Potassium Triflate and a Europium -diketonate Complex. ECS Trans 61:213–225. https://doi.org/10.1149/06105.0213ecst